IEEE Access
Multidisciplinary | Rapid Review | Open Access Journal

Date of publication xxxx 00, 0000, date of current version xxxx 00, 0000.

Digital Object Identifier 10.1109/ACCESS.2017.Doi Number

Loss Characterization of Giant Magnetostrictive Material under Compressive Stress

Yukai Chen[1], Xin Yang[1], Member, IEEE, Zhihe Zhang[1], Yanfei Wei[1], and Haobin Zheng[1]

[1] College of Electrical and Information Engineering, Hunan University, Changsha 410082, China;

Corresponding author: Xin Yang (e-mail: yangxin.cambridge@foxmail.com).

This work was supported by the Huxiang High-level Talent Gathering Project, grant number 2019RS1028.

ABSTRACT The properties of giant magnetostrictive material (GMM) are very sensitive to external compressive stress. Knowledge of these key properties is of essential importance in practical applications such as high-power underwater transducers. Although the parameters of GMM have been extensively studied, characterization and analysis of magnetic, elastic, and piezoelectric losses under different compressive stresses are rarely reported due to the difficulty in experimentally realizing the ideal mechanical free or clamped boundary conditions. In this study, we designed a longitudinal transducer for complex parameters characterization of GMM. We successfully characterize the key three losses in GMM using a multi-degree-of-freedom (MDOF) lumped parameter equivalent circuit model (LECM), meticulously incorporating the surface contact damping, stiffness, and structural losses. MDOF LECM provides a novel idea for loss characterization of GMM under compressive stress. In contrast to prior-art parameters characterization based on the distributed parameter equivalent circuit model (DECM), the proposed characterization based on MDOF LECM shows apparent superiority in terms of global sensitivity. The intensive losses of GMM for ten-time characterizations show high stability and are all positive. Statistical analysis of intensive losses' dependency on the compressive stress is performed. A longitudinal transducer is designed for experimental verification. Finally, 95% prediction and confidence intervals for the variation trend of the intensive losses in relationship with compressive stress are obtained.

INDEX TERMS Giant magnetostrictive material (GMM); Intensive Loss; Compressive Stress; Multi-degree-of-freedom (MDOF); Lumped-parameter Equivalent Circuit Model (LECM)

I. INTRODUCTION

High-power giant magnetostrictive devices, such as underwater transducers and smart actuators, have been widely used in marine engineering and aerospace in recent years [1]–[5]. Evaluating the heat generated by a device has become a crucial part of practical applications [6]–[8]. The main factor that generates heat is the losses of GMM: magnetic losses, elastic losses, and piezoelectric losses [9]. Similar to piezoelectric materials, according to the magnetic and mechanical boundary conditions of GMMs [2], the losses of GMM are further divided into "intensive" and "extensive" losses [7], [9], and the corresponding material complex parameters are shown in equations (1) and (2).

$$\begin{cases} \mu^{\sigma*} = \mu^{\sigma}(1 - j\tan\delta') \\ S^{\mathrm{H}*} = S^{\mathrm{H}}(1 - j\tan\phi') \\ d^{*} = d(1 - j\tan\theta') \end{cases} \quad (1) \qquad \begin{cases} \upsilon^{\mathrm{s}*} = \upsilon^{\mathrm{s}}(1 + j\tan\delta) \\ c^{\mathrm{B}*} = c^{\mathrm{B}}(1 + j\tan\phi) \\ h^{*} = h(1 + j\tan\theta) \end{cases} \quad (2)$$

In Equation (1), $\mu^{\sigma*}$ is stress (σ)-constant complex permeability, $S^{\mathrm{H}*}$ is magnetic field (H)-constant elastic compliance, d^{*} is complex piezoelectric coefficient. $\tan\delta'$, $\tan\phi'$ and $\tan\theta'$ are the magnetic, elastic and piezoelectric loss tangents, respectively, which are "intensive" losses. In Equation (2), $\upsilon^{\mathrm{s}*}$ is strain (s)-constant inverse complex permeability, $c^{\mathrm{B}*}$ is magnetic induction (B)-constant elastic stiffness, h^{*} is the inverse complex piezoelectric constant d^{*}.And $\tan\delta$, $\tan\phi$ and $\tan\theta$ are "extensive" losses.

The "intensive" and "extensive" losses correspond to two distinct magnetic and mechanical boundary conditions. According to the direction of the loss hysteresis loop, intensive losses are negative signs and extensive losses are positive signs, which is also a mathematical convention [10]. Usually, intensive losses could be used in finite element model (FEM) simulation for response analysis of transducers [11][12].

The parameters of GMM considering losses are very sensitive to compressive stress, which is required in practical applications [13]. Although many researchers have explored the relationship between the permeability, compliance coefficient, and piezomagnetic coefficient (real parts) of GMM with compressive stress [13], [14], the three types of losses (imaginary parts) are rarely discussed. Greenough and Reed et al. [15], [16] first characterized three losses of GMMs by complex material quantities. They measured the impedance curve of a "free-stand" GMM rod without compressive stress, established a plane wave model (PWM) under the boundary of σ-constant and B-constant, and extracted the real and imaginary parts (losses) of the complex parameters of the GMM rod through intelligent algorithms. However, the losses obtained by this method are under zero compressive stress, which greatly deviates from the application. Greenough et al. [17] then applied disc springs to apply compressive stress to a GMM rod, and used the same PWM to extract the material losses at 5 Mpa. However, the signs of obtained imaginary parts appear to be abnormal, which contradicts the theoretical expectation. This is because all the losses of the device are "integrated" into the material losses. When investigating on the effect of compressive stress on material properties, it is inevitable to introduce compressive stress-applying devices (e.g., disc springs, stress rods, and masses) [18], so the measured impedance is the performance of the entire device, instead of individual material properties [17], [19], [20]. Therefore, such a transducer for material parameter characterization not only has material loss, but also the structural damping losses of the mechanical components and the friction losses of the contact surface [21], [22]. In [21], structural losses and friction losses account for 45.7% and 45.3% of the total transducer losses, respectively, so these losses cannot be ignored. When studying material losses under compressive pressure, it is necessary to separate the properties of materials and devices [17], [18], [21].

In the field of piezoelectric materials which are also widely used in marine and aerospace[23]–[26], there have been a variety of methods to characterize the losses of materials [19], [20], [27]. Some researchers have measured the impedance curves of piezoelectric materials and constructed equivalent circuits, which are an effective way to study piezoelectric materials[28]–[30]. The difference between 1D model [31]–[34] or the 2D and 3D FEM data [35], [36] between experimental data is then minimized by intelligent algorithms. This kind of methods is also called the iterative method. Other researchers have designed non-iterative methods to measure and calculate complex parameters at characteristic frequencies[10], [37], [38]. In addition, some researchers combine iterative and non-iterative methods to characterize all the complex parameters of materials [39], [40].

However, most studies on piezoelectric materials are still carried out under the mechanical free boundary of the material without compressive stress, which means that the losses under zero compressive stress are characterized [21]-[34]. This is mainly due to the requirement to eliminate the clamping effect caused by the compressive stress from the applying device, which increases the complexity of the experiment and makes it difficult to achieve ideal σ-constant boundary conditions [18], [41]. In the latest research, Daneshpajooh et al.[18] has made great progress in the study of the piezoelectric losses under compressive stress. A piezoelectric transducer is carefully designed to overcome the clamping effect so that both ends of the transducer have σ-constant boundaries. Based on PWM, the effects of compressive stress on dielectric, elastic, and piezoelectric losses are more accurately characterized. In [42], a longitudinal vibration transducer with a free boundary at one end and a clamped boundary at the other is developed. The structural damping of the transducer and the contact damping of the interface are measured and calculated to thus separate the device losses and material losses. However, only a single-degree-of-freedom lumped-parameter model is used. The GMM rod, magnetic column, and displacement plunger of the transducer are assumed to move at the same velocity. As a result, the accuracy of the scheme is greatly undermined.

In this study, an MDOF LECM that meticulously incorporates the surface contact damping and stiffness is innovatively established to improve the accuracy of the impedance simulation. The model can reflect the effect of contact damping and stiffness on the motion state of each degree of freedom in the transducer. The global sensitivity and stability of parameter characterization by using the newly proposed MDOF LECM and the classical DECM (also known as the PWM) were compared. The proposed MDOF LECM performs well in terms of global sensitivity of parameters and stability of characterization. Finally, through statistical analysis, 95% prediction and confidence intervals are calculated for the variation trend of the intensive losses under different compressive stress.

II. DEVICES AND EXPERIMENTS

Herein, a longitudinal transducer with one end bounded and one end free was designed and fabricated as the material characterization device. The impedance test, the contact damping and stiffness test of the main contact surface, and the structural damping test of the displacement plunger were carried out.

A. THE LONGITUDINAL TRANSDUCER DESIGN

A screw-clamped longitudinal vibration transducer is

designed to characterize the material parameters of the k_{33} mode under different compressive stress, the schematic diagram of which is shown in Fig. 2(a). To remove the clamping effect [18], eight spring washers between the stainless steel pre-tightening end cover and the displacement plunger are placed. Compressive stress is applied through pre-stress adjusting screws while the free vibration boundary condition for the GMM rod can be maintained. A 20×100 mm GMM rod with a high length/radius ratio is used as the characterization sample. On one hand, samples with a high length/radius ratio can keep the fundamental longitudinally resonance away from higher resonance frequencies; on the other hand, it can more easily eliminate the clamping effect, so that the k_{33} vibration mode can be obtained without interference or spurious modes.

FEM is used to analyze the magnetic field distribution inside the GMM rod. The DC solenoid is 1540 turns, the DC is 2 A, the AC solenoid is 940 turns, the effective value of the AC is 0.02 A, and the frequency is 1600 Hz. It can be seen from Fig. 1(a) that most of the magnetic lines form a closed magnetic circuit through the magnet block, the GMM rod, the magnetic return path disc, the magnetic return path cylinder, and the housing base. Due to the low magnetic permeability of the GMM, part of the leakage magnetic lines pass through the gap between the coil and the GMM rod, as shown in Fig.1(a). The magnetic field must be corrected. According to [43], the magnetic flux leakage coefficient k_m^2 =0.9205 is calculated.

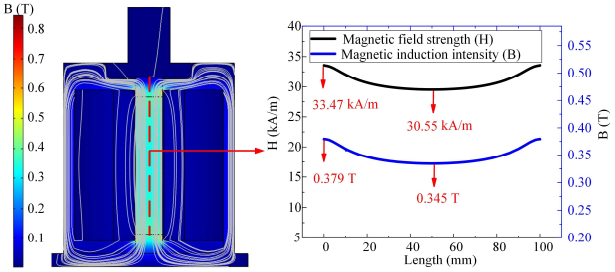

FIGURE 1. (a)The distribution of B and magnetic lines; (b)The value of the H and B of the central axis of the GMM rod

The magnetic field strength (H) and magnetic induction intensity (B) of the central axis of the GMM rod (red dotted line in Fig. 1(a)) are calculated, and both H and B are distributed symmetrically about the center point of the GMM rod (Fig. 1(b)). The difference between the maximum and minimum H is 8.7% and that for B is 8.9%. Therefore, the magnetic field in the axial direction of the GMM rod can be approximately regarded as a uniform distribution. So that the spatial distribution of the magnetic field is ignored in this study. Based on the assumption that the magnetic field is uniformly distributed, $H=NI/l_G$ is used to calculate the equivalent magnetic field of the GMM rod in the modeling in Section III, where H represents the axial magnetic field strength, N represents the number of turns of the solenoid, I represents the excitation current, and l_G represents the length of the GMM rod.

B. EXPERIMENTAL MEASUREMENT

The base of the longitudinal transducer is fixed on the shock-absorbing table, so the end of the GMM rod connected to the base is the clamped boundary condition, and the other end is the free boundary condition. Use an impedance analyzer (KEYSIGHT E4990A) to connect the AC solenoid (940 turns) to measure the impedance/phase data of the longitudinal transducer. The programmable DC power supply (RIGOL DP832) is connected to the DC solenoid (1540 turns) and provides 2 A DC. The compressive stress is applied by turning the screws, and the values of the compressive stress are precisely measured using a ring pressure sensor (YAOHUA XK3190). The impedance/phase curves of six groups of different compressive stresses were measured respectively. The detailed measurement procedure of the structural damping of the displacement plunger and the detailed calculation formulas for the contact damping and stiffness were described in a previous study [42].

III. MODELS AND METHOD

A MDOF mechanical model and a distributed mechanical model are both constructed for the longitudinal transducer, and then the parameters and losses of the GMM rod are characterized based on the two aforementioned models by particle swarm optimization (PSO) algorithm.

A. MDOF MECHANICAL MODEL AND MDOF LECM

There are multiple contact surfaces in the transducer. For the longitudinal transducer with one end clamped and one end free in this study, the most important contact surfaces are the contact surfaces of the GMM rod and the magnetic column (G-M surface), and the contact surfaces of the magnetic column and the displacement plunger (M-D surface) as shown in Fig. 2 (a) indicated by the red circle. Their surface morphology was measured using Bruker's Contour Elite 3D microscope and is shown on the left of Fig. 2(a). The normal contact model of the contact surface is equivalent to a spring and a viscous damper [44]–[48]. This means that there is energy storage and dissipation at the contact surfaces [44]–[48], and the two rough surfaces that make up the contact surface have unequal velocities.

Considering the normal stiffness and contact damping of the contact surface, an MDOF mechanical model as shown in Fig. 2(b) is established. $K_{C\text{-}M}$ and $K_{M\text{-}D}$ represent the normal equivalent stiffness of the G-M surface and the M-D surface, respectively. $R_{C\text{-}M}$ and $R_{M\text{-}D}$ represent the contact damping of G-M surface and M-D surface. M_D, M_C, and M_G are the actual mass of the displacement plunger, magnetic column, and GMM. K_{spr} and K_{GMM} represent the stiffness of the spring washers and GMM. R_G is the mechanical damping of the GMM. x_1, x_2, and x_3 are the displacements

of the GMM rod, magnetic column and displacement plunger, respectively. Therefore, the velocities at both ends of the G-M surface are $\dot{x}_1$ and $\dot{x}_2$. The velocities at both ends of the M-D surface are respectively for $\dot{x}_2$ and $\dot{x}_3$.

In this transducer device, the stiffness of the magnetic column and the displacement plunger are much greater than that of the GMM rod, so in the MDOF mechanical model, the magnetic column and the displacement plunger are equivalent to ideal rigid bodies without compression and bending. One end of the GMM connected to the bass is clamped, and the velocity is zero. According to the kinetic energy conservation law, the equivalent mass of the GMM rod is calculated to be one-third of the actual mass. At the same time, there are non-negligible mechanical losses of GMM, so in the MDOF mechanical model, the GMM rod is equivalent to a spring with mass and damping.

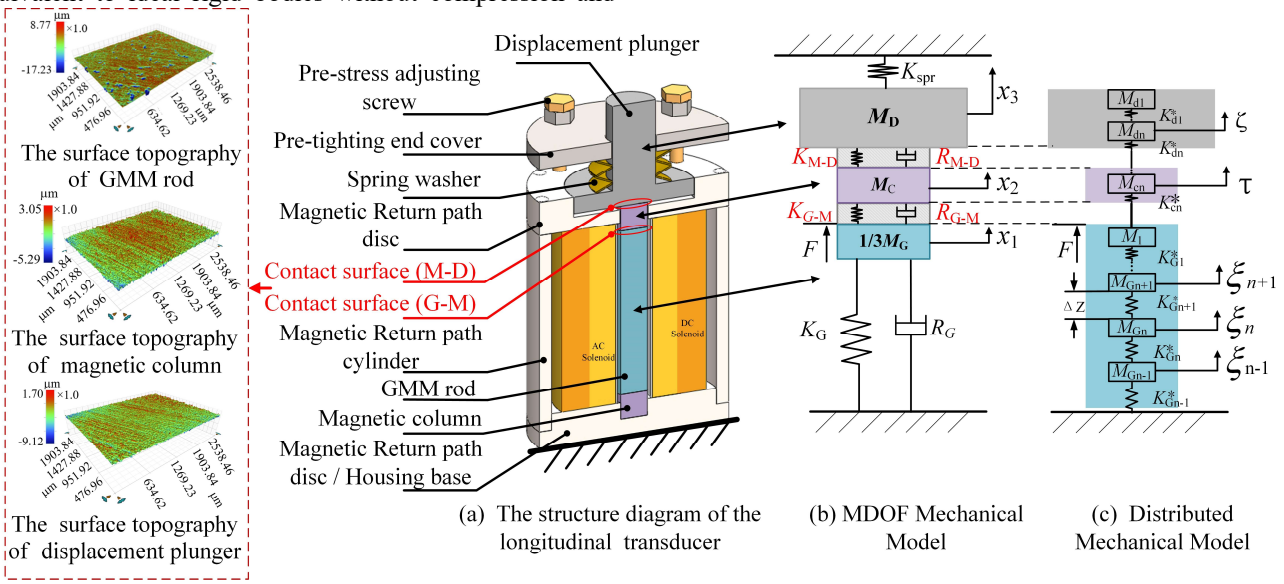

FIGURE 2. The structural diagram of the longitudinal transducer and two mechanical models.

Based on the MDOF mechanical model shown in Fig. 2(b), the equation of motion is established as follows [49]:

$$\begin{cases} Fe^{j\omega t} = M_G\ddot{x}_1/3 + K_G x_1 + R_G\dot{x}_1 + K_{G\text{-}M}(x_1 - x_2) + R_{G\text{-}M}(\dot{x}_1 - \dot{x}_2) \\ 0 = M_C\ddot{x}_2 + K_{M\text{-}D}(x_2 - x_3) + R_{M\text{-}D}(\dot{x}_2 - \dot{x}_3) - K_{G\text{-}M}(x_1 - x_2) - R_{G\text{-}M}(\dot{x}_1 - \dot{x}_2) \\ 0 = M_D\ddot{x}_3 + K_{spr}x_3 - K_{M\text{-}D}(x_2 - x_3) - R_{M\text{-}D}(\dot{x}_2 - \dot{x}_3) \end{cases} \quad (2)$$

According to the impedance analogy: mass is analogous to inductance, and velocity is analogous to current. So the equivalent circuit equation of the mechanical part is as follows:

$$\begin{cases} F = j\omega M_G v_1/3 + K_G v_1/j\omega + R_G v_1 + K_{G\text{-}M}(v_1 - v_2)/j\omega + R_{G\text{-}M}(v_1 - v_2) \\ 0 = j\omega M_C v_2 + K_{M\text{-}D}(v_2 - v_3)/j\omega + R_{M\text{-}D}(v_2 - v_3) - K_{G\text{-}M}(v_1 - v_2)/j\omega - R_{G\text{-}M}(v_1 - v_2) \\ 0 = j\omega M_D v_3 + K_{spr}v_3/j\omega - K_{M\text{-}D}(v_2 - v_3)/j\omega - R_{M\text{-}D}(v_2 - v_3) \end{cases} \quad (3)$$

Combined with the theory of electro-mechanical conversion [2], [50], the MDOF LECM is obtained as shown in Fig.3. Among them, the permeability $\mu_{33}^{\sigma^*}$, compliance coefficient $S_{33}^{H^*}$ and coupling coefficient d_{33}^* of GMM rod are all complex numbers [9].

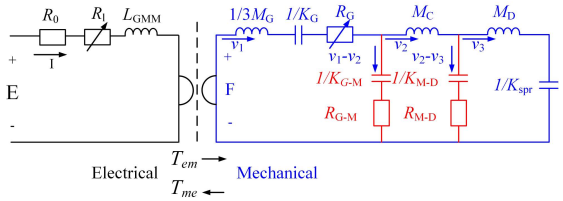

FIGURE 3. The Schematic of MDOF LECM for the longitudinal transducer

The left side of the circuit represents the electrical part and the right side represents the mechanical part. Electrical elements and mechanical elements can be converted to each other by the conversion factor T_{em}/T_{me}. The expression for the conversion factor is:

$$T_{em} = -T_{me} = NA_G d_{33}^* / S_{33}^{H^*} l_G \quad (4)$$

Among them, N, A, and l_G represent the number of turns of the excitation solenoid, the cross-sectional area and length of the GMM rod, respectively.

The impedance Z_{e1} of the electrical part is expressed as:

$$Z_{e1} = R_0 + j\omega((R_l + j\omega L_{GMM})/j\omega) \quad (5)$$

where R_0 represents the DC impedance of the solenoid, R_l represents the frequency-dependent impedance caused by magnetic losses of GMM, and its expression is Eq. (6). $L_{GMM}=\chi_r L_b$, L_b represents the inductance of the wound solenoid when the GMM is clamped, and its expression is Eq. (6).

$$R_l = -\omega(\chi_i - \tan\delta_{33}^{'})L_b \quad (6)$$

$$L_b = (1-(k_{33}^*)^2)\mu_{33}^{'}N^2 A_G / l_G \quad (7)$$

where χ_r and χ_i are the real and imaginary parts of the eddy factor, respectively [51].

$k_{33}^* = \sqrt{(d_{33}^2)^*/(\mu_{33}^{\sigma^*}S_{33}^{H^*})}$ respects the magneto-mechanical coupling.

The impedance Z_{t1} of the mechanical part is expressed as:

$$Z_{t1}=[(j\omega M_D+\frac{K_{spr}}{j\omega})//(\frac{K_{M\text{-}D}}{j\omega}+R_{M\text{-}D})+j\omega M_C]//(\frac{K_{G\text{-}M}}{j\omega}+R_{G\text{-}M})+j\omega\frac{M_G}{3}+\frac{K_G}{j\omega}+R_G \quad (8)$$

The transducer's electrical impedance frequency response function Z_1 is given as follows:

$$Z_1=Z_{e1}-T_{em}T_{me}/Z_{t1} \quad (9)$$

The equation of phase P_1 is:

$$P_1=\arctan(\frac{\mathrm{img}(Z_1)}{\mathrm{real}(Z_1)})\frac{180}{\pi} \quad (10)$$

B. DISTRIBUTED MECHANICAL MODEL AND DECM

Fig.2(c) shows a distributed mechanical model of the transducer. In the distributed model, the displacement plunger, magnetic column, and GMM rod are divided into n adjacent small lumped elements Δ Z, Δ Z=L/n. L represents the length of the object. Since the element ΔZ is much smaller than the wavelength, it can be represented as a mass and a spring. M_{Gx} and K^*_{Gx} （x=1,2,⋯n） represent the mass and complex stiffness of each element in the GMM rod, and ξ_x represents the longitudinal displacement of the xth element of the GMM rod. M_{Cx} and K^*_{cx} （x=1,2,⋯n） are the mass and complex stiffness of each element in the magnetic column, respectively. τ_x represents the longitudinal displacement of the xth element of the magnetic column. M_{Dx} and K^*_{Dx} (x=1,2,⋯n) represent the mass and complex stiffness of each element in the displacement plunger, and ζ_x represents the longitudinal displacement of the xth element of the displacement plunger.

In the distributed parameter model, the contact surface is rarely considered [2]. The velocities at both ends of the contact surface are normally treated to be equal, so the displacement plunger, magnetic column, and GMM rod are directly connected in series within the distributed mechanical model [2].

The corresponding DECM is shown in Fig.4. The detailed derivation process is shown in Appendix A [2]. Based on algebraic operations, the equivalent circuit of the mechanical side is usually represented by a "T network". The expressions for each element are shown in (11)-(15).

$$Z_G=-j\rho_G c_G A_G\cot k_G L_G \quad (11)$$

$$Z_{C1}=j\rho_c c_c A_c\tan(k_c l_c/2) \quad (12)$$

$$Z_{C2}=-j\rho_c c_c A_c/\sin(k_c l_c) \quad (13)$$

$$Z_{D1}=j\rho_d c_d A_d\tan(k_d l_d/2) \quad (14)$$

$$Z_{D2}=-j\rho_d c_d A_d/\sin(k_d l_d) \quad (15)$$

The subscript "G" stands for GMM rod, the subscript "C" stands for the magnetic column, the subscript "D" for the displacement plunger, and ρ, c, k, A, and L stand for density, wave velocity, wave number, cross-section, and length, respectively. The wave speed is expressed as $c=1/\sqrt{\rho S^{H*}_{33}}$, and the wave number is $k=\omega/c$.

The impedance Z_{t2} of the mechanical part is expressed as:

$$Z_{t2}=(Z_{D1}//Z_{D2}+Z_{D1}+Z_{C1})//Z_{C2}+Z_{C1}+Z_G+\varphi^2(R_l+L_{GMM}) \quad (16)$$

The transducer's electrical impedance frequency response function Z_2 is given as follows:

$$Z_2=R_0+(R_1+j\omega L_{GMM})//[Z_{t2}/(T_{em}/\omega L_{GMM})^2] \quad (17)$$

The equation of phase P_2 is:

$$P_2=\arctan(\frac{\mathrm{img}(Z_2)}{\mathrm{real}(Z_2)})\frac{180}{\pi} \quad (18)$$

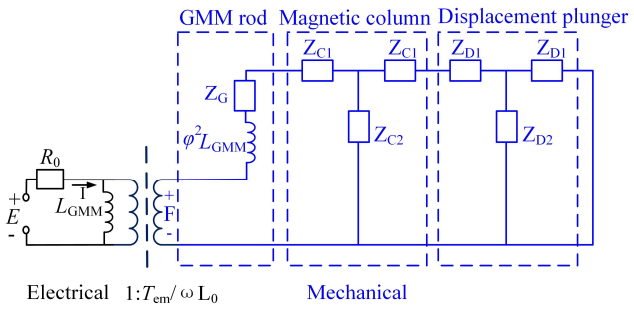

FIGURE 4. The Schematic of DECM for the longitudinal transducer

C. THE CHARACTERIZATION METHOD

In this paper, the material parameters and losses are characterized by parameter identification. The PSO algorithm is used iteratively to find the unknowns that minimize the value of fitness function. Three different parameter characterization methods are compared.

Method A is based on the MDOF LECM, and the process of characterization can be divided into two steps. The first step determines the real parts of the three complex parameters, and sets the unknowns to be identified as $\partial_1=[\mu'_{33}\ d'_{33}\ S'_{33}]^T$ and $\partial_2=[\tan\delta'_{33}\ \tan\phi'_{33}\ \tan\theta'_{33}]^T$. Eq. (9) is used to generate the simulated electrical impedance, denoted as $\hat{Z}_A(i,\partial_1,\partial_2)$, and the experimentally measured impedance modulus value is denoted as $Z(i)$. The fitness function $F_{ZA}(i)$ of PSO is shown in Eq. (19), which is the root mean square error (RMSE) between experimental impedance data and simulated impedance data. I represent the total number of sampling points, and i represent the ith sampling point. The identified $\hat{\partial}_1$ is the real part of the complex parameter and is used as the known number in the second step, and the identified ∂_2 is discarded. The second step determines the three losses of the material. Setting the unknown in the model as $\gamma=[\tan\delta'_{33}\ \tan\phi'_{33}\ \tan\theta'_{33}]^T$, Eq.(10) is used to generate the simulated phase, denoted as $\hat{P}_A(i,\gamma)$, and the experimentally measured impedance modulus value as $F_{pA}(i)$. The fitness function of parameter identification is shown in Eq. (20), which is the RMSE between the experimental phase and the simulated phase data.

Method B is based on the DECM, which is also the same as method A to determine the complex parameters of the material in two steps. Equations (17) and (18) are used to generate the simulated electrical impedance and simulated phase, denoted as $\hat{Z}_B(i,\partial_1,\partial_2)$ and $\hat{P}_B(i,\gamma)$, respectively.

The fitness function of the first step is $F_{zB}(i)$, as shown in Eq. (21), and the fitness function of the second step is $F_{pB}(i)$, as shown in Eq. (22).

Method C is also based on the DECM, but the complex parameters are determined in only one step of identification, which is also a classic method. That is, ∂_1 and ∂_2 are identified by the fitness function $F_{zC}(i) = F_{zB}(i)$, are used as the final result for the real and imaginary parts of the complex parameters, respectively.

$$F_{zA}(i)=\sqrt{\frac{1}{I}\sum_{i}^{I}(Z(i)-\hat{Z}_A(i,\partial_1,\partial_2))^2} \quad (19)$$

$$F_{pA}(i)=\sqrt{\frac{1}{I}\sum_{i}^{I}(P(i)-\hat{P}_A(i,\gamma))^2} \quad (20)$$

$$F_{zB}(i)=\sqrt{\frac{1}{I}\sum_{i}^{I}(Z_B(i)-\hat{Z}_B(i,\partial_1,\partial_2))^2} \quad (21)$$

$$F_{pB}(i)=\sqrt{\frac{1}{I}\sum_{i}^{I}(P(i)-\hat{P}_B(i,\delta))^2} \quad (22)$$

IV. EXPERIMENT RESULTS

The impedance curves of longitudinal vibration transducers under 6 groups of compressive stress (6.0Mpa, 10.0Mpa, 17.5Mpa, 20.8Mpa, 25.3Mpa, 30.0Mpa) were measured respectively. The real and imaginary parts (losses) of the complex parameters were characterized by methods A-C, respectively. To compare the three methods, the data of 10.0 Mpa is selected as an example, and the global sensitivity analysis and stability analysis of parameter characterization are carried out.

A. GLOBAL SENSITIVITIES ANALYSIS

For comparison, the characterization results based on the two fitness functions were normalized, and all parameter values were divided by the corresponding minimum of fitness. And the width ΔF is used to quantify the sensitivity when the normalized fitness value =1.1.

The effects of methods A-C were assessed by global sensitivity analysis. If the fitness function value is more sensitive to one parameter, the identified parameter is closer to its true value. Therefore, sensitivity analysis helps in rational selection and judgment of parameter identification results when the true value is unknown [52], [53]. Usually, a scatter plot of the parameter distribution during the algorithm iteration is drawn to show the sensitivity. The sharpness at the bottom of the scatterplot reflects the sensitivity of the fitness function to the parameters [34].

Fig. 5 shows the scatter plots of the three methods to identify material parameters and losses at 10.0 Mpa. The red, blue, and black scatter represent Methods A-C, respectively. To facilitate comparison, normalization is performed: all fitness values are divided by the minimum fitness value, and the parameter value to be determined is divided by the average number of the search range. The abscissa and ordinate represent the normalized parameter value and fitness value, respectively.

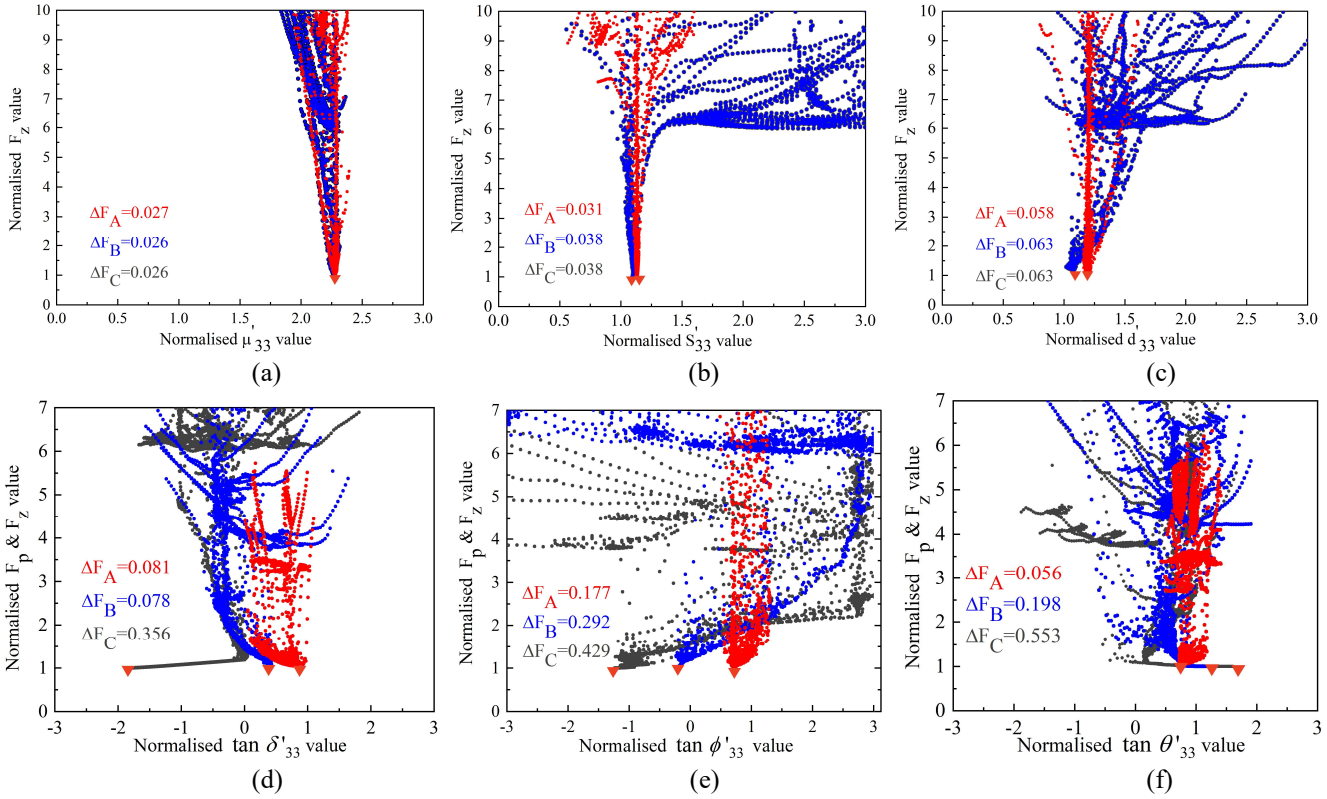

FIGURE 5. Sensitivities of six parameters in methods A-C. Δ F is defined in the text and is used to quantify global sensitivity.

Red triangles are used to represent local minima. And using the width ΔF at normalized fitness value = 1.1 to quantify the sensitivity, the quantified value is written in Fig. 5. The smaller the ΔF, the higher the sensitivity of the fitness function to this parameter.

It can be seen from Fig.5 (a-c) that the fitness functions of methods A-C are all highly sensitive to μ_{33}', S_{33}', and d_{33}', and ΔF of the three methods are similar. This shows that all three methods can extract the real part of the parameter that is closer to the true value. In addition, methods B and C are the same way to characterize the real part of material parameters, so their scatter points are coincident.

However, the sensitivities of the fitness functions of the three methods to $\tan\delta_{33}^{'}$, $\tan\phi_{33}^{'}$ and $\tan\theta_{33}^{'}$ are quite different (Fig. 5(d-f)). Among them, method C has the lowest sensitivity, and the basin of the scatter plot is almost flat, indicating that the loss value represented by method C is less reliable. The fitness value of method B has a high sensitivity to $\tan\delta_{33}^{'}$, which is greatly improved compared to method C, but the sensitivity to $\tan\phi_{33}^{'}$ and $\tan\theta_{33}^{'}$ is still very low, indicating that method B cannot obtain reliable values. Note that the fitness function of Method A is much more sensitive to all three losses, and ΔF of each parameter is ten times smaller than that of method C. Therefore, Method A characterizes more reliable three losses of GMM under compressive stress.

B. STABILITY AND REPEATABILITY

Based on methods A-C, 10 random parameter extractions were performed, and the stability of the three methods was analyzed [54]. This is a commonly used way to analyze the effect of parameter identification. The parameter settings of the PSO algorithm in the three methods remain the same, in which the learning factor c_1=c_2=2, and the inertia weight w=0.5, the particle swarm size is 12.

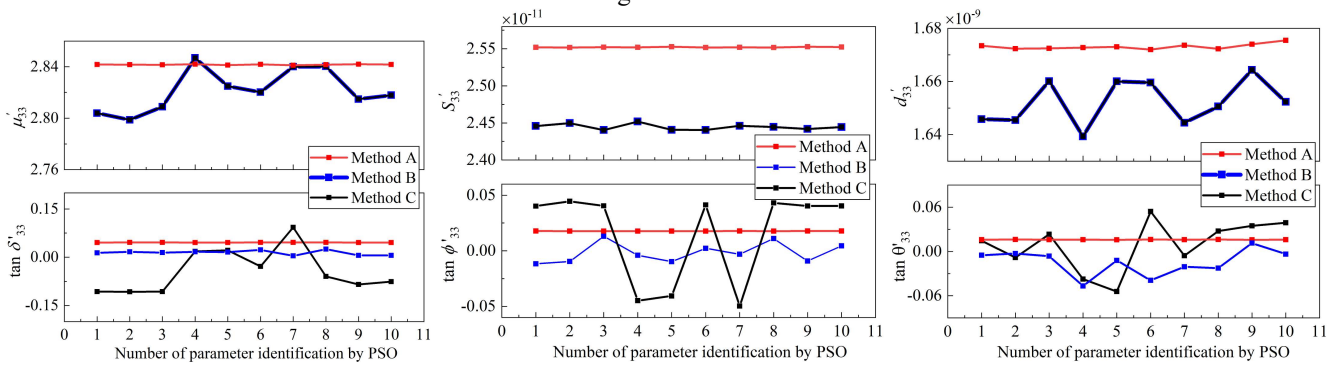

FIGURE 6. Comparison of the results of ten extractions with the three different methods at 10 Mpa.

TABLE I
EXTRACTION RESULTS AND THE COEFFICIENTS OF VARIATION FOR SIX PARAMETERS

Parameter	Search Range	Method A		Method B		Method C	
		$\bar{x}$	$\lvert cv\rvert$%	$\bar{x}$	$\lvert cv\rvert$%	$\bar{x}$	$\lvert cv\rvert$%
$\mu_{33}^{'}$	[2,3]	2.842	9.523×10^{-5}	2.822	0.006	2.822	0.006
$S_{33}^{'}$	$[1\times10^{-12}, 1\times10^{-10}]$	2.552×10^{-11}	1.499×10^{-4}	2.445×10^{-11}	0.002	2.445×10^{-11}	0.002
$d_{33}^{'}$	$[5\times10^{-10}, 5\times10^{-9}]$	1.673×10^{-9}	6.231×10^{-4}	1.652×10^{-9}	0.005	1.654×10^{-9}	0.007
$\tan\delta_{33}^{'}$	[−0.1, 0.1]	0.045	0.005	0.014	0.505	−0.043	1.560
$\tan\phi_{33}^{'}$	[−0.1, 0.1]	0.018	0.003	−0.002	5.334	0.015	2.706
$\tan\theta_{33}^{'}$	[−0.1, 0.1]	0.016	0.008	−0.015	1.202	0.009	3.937

Fig.6 shows the results of 10 parameter identifications for methods A-C. The results show that the stability of the real part of the parameters identified by the three methods is relatively high. However, the elastic losses and piezomagnetic losses identified by methods B and C have poor stability, and the loss value fluctuates between positive and negative values. This is untrue, particularly under small-signal excitation. The three losses extracted by Method A have the highest stability. Stability is quantified using the coefficient of variation, calculated as $cv=(\psi/\eta)\times100\%$.ψ represents the standard deviation, and η represents the mean of the set of data.

The mean value of 10 identifications of the complex parameters of the material at 10.0 Mpa, the absolute value of the coefficient of variation, and the parameter search range are all listed in Table 1. Method A has the lowest coefficient of variation for 10 times of loss identification, indicating the highest stability. The coefficient of variation corresponding to methods A-C also has a similar law to the sensitivity. The smaller the sensitivity ΔF, the smaller the coefficient of variation, indicating that the extracted parameters are more reliable and closer to the true value.

C. SIMULATION AND EXPERIMENTS

Fig. 7 shows the comparison between the simulation data and the experimental data at 10 Mpa. Fig.8 is the RMSE between the simulated data and the experimental data under different compressive stresses.

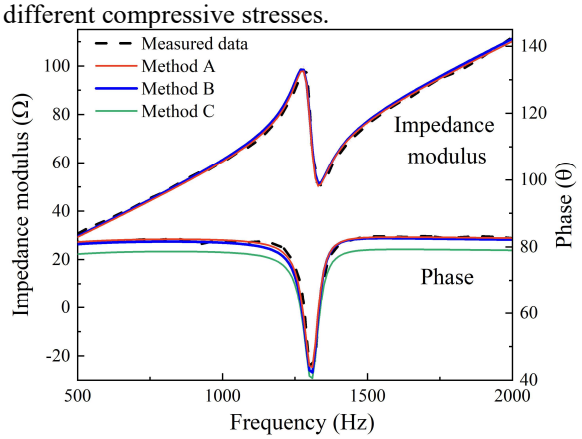

FIGURE 7. Comparison of the experimental data and simulation data under compressive stresses of 10.0 Mpa

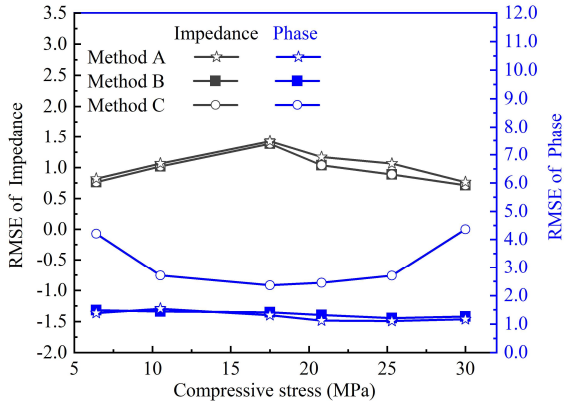

FIGURE 8. RMSE of parameter extraction under different compressive stresses

Simulations were performed using the parameters characterized by method A. The simulated impedance modulus and phase obtained were in excellent agreement with the experimental curves (Fig. 7), and RMSEs is 1.06 and 1.53, respectively (Fig. 8). Similarly, for simulations using the parameters characterized by method B, the model data and experimental data also have a high degree of similarity, and almost coincide with the curves obtained by method A (Fig. 7). However, according to Fig. 6 and TABLE I, it can be seen that the material losses represented by method B have negative values and poor stability. This shows that although method B makes the model fit well, the loss value of the characterization is abnormal.

For method C, the simulated impedance data were consistent with the experimental data (Fig.7) with an RMSE of 1.08 (Fig.8). But the simulated phase data are significantly different from the experimental data and the simulated data are smaller than the experimental phase data (Fig.7), and the RMSE between them is 2.81 (Fig.8). This also illustrates that Method C cannot reliably characterize the losses of the GMM.

The above results show that we need to comprehensively consider sensitivity, stability, and simulation to judge the quality of the three methods, and the best method is method A as expected. In addition, Fig.8 shows that the RMSEs under different compressive stresses all satisfy the above rules.

D. PARAMETER CHARACTERIZATION RESULTS

Based on method A, material parameters and loss tangent values under different compressive stress were identified, and polynomial fitting was performed on the extracted results.

The goodness of fit R^2 was used to evaluate how well the model fits the experimental values. R^2=SSR/SST, where: SST is the total sum of squares, and SSR is the regression sum of squares.

Let Y(P) represent the complex parameter of the GMM and P represent the pressure, the possible models of Y(P) are:

$$Y(P)= B_0+B_1\times P+ B_2\times P^2+ B_2\times P^3 \quad (23)$$

where B_i is the coefficients of the polynomial model. TABLE II lists the model coefficients of the polynomial corresponding to each parameter and the model goodness of fit R^2.

TABLE II
COEFFICIENTS (B_i) AND GOODNESS OF FIT (R^2) IN THE FITTED MODEL

Parameter	B_0	B_1	B_2	B_3	R^2
$\mu'_{33}(P)$	2.5308	0.0625	-0.0038	6.1175e-5	0.9957
$S'_{33}(P)$	3.1579e-11	-4.4633e-13	-2.6327e-14	8.2555e-16	0.9904
$d'_{33}(P)$	1.8080e-9	4.0171e-11	-6.6146e-12	1.3233e-13	0.9991
$\tan\delta'_{33}(P)$	-0.0431	-0.0013	1.2373e-4	-2.0833e-6	0.9942
$\tan\phi'_{33}(P)$	-0.0772	0.0093	-4.1132e-4	5.9555e-6	0.9973
$\tan\theta'_{33}(P)$	-0.0372	0.0033	-1.5028e-4	2.2872e-6	0.9833

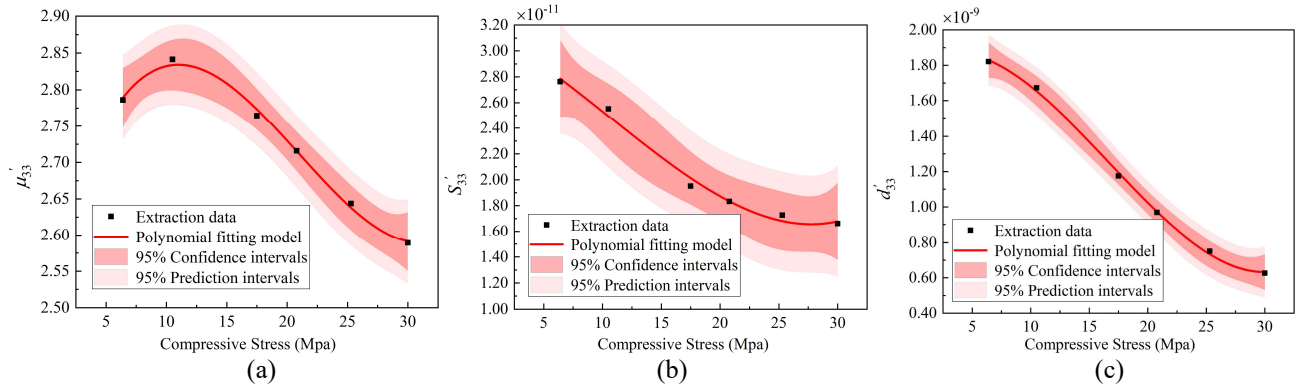

FIGURE 9. Variation of real part of parameters with different compressive stress and fitting model

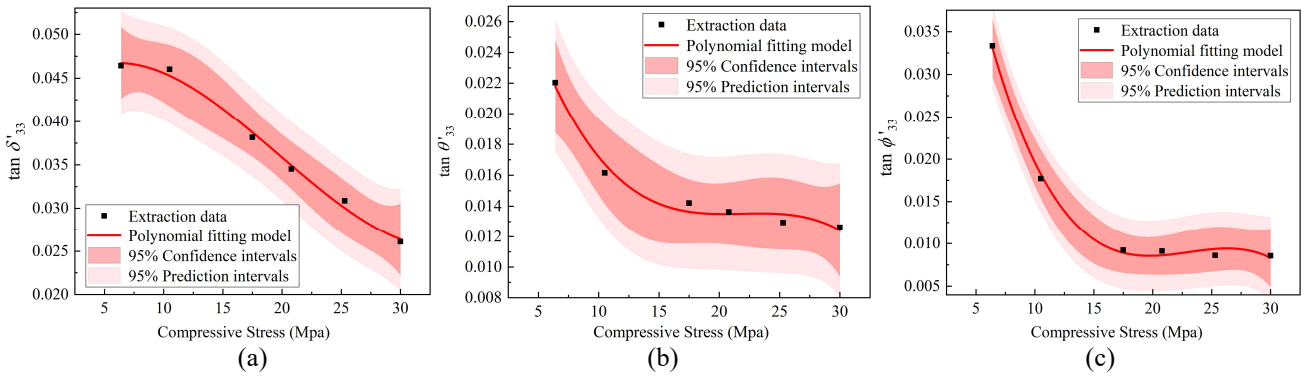

FIGURE 10. Variation of losses tangent with different compressive stress and fitting model

Figures 9 and 10 plot the material real parameters and losses at different compressive stresses, the fitted model curves, and the 95% confidence and prediction intervals calculated from the standard error of the polynomial fit. This means that there is a 95% confidence that the average complex parameters of the GMM rod are within the confidence interval. Likewise, 95 out of 100 times, the complex parameters of any individual GMM will lie within the prediction interval.

According to Fig. 9, the magnetic permeability of the material first increases and then decreases with the compressive stress (6-30 Mpa), and both the compliance coefficient and the piezomagnetic coupling coefficient decrease with the compressive stress, which is consistent with that reported in previous measurements [55].

Fig.10 reports a model of the relationship between material losses and compressive stress, observing that the magnetic losses decrease monotonically with compressive stress.

In addition, in the range of 6-15Mpa, the elastic and the piezomagnetic coupling losses decrease monotonically. When the compressive stress is greater than 15Mpa, the elastic and the piezomagnetic coupling losses gradually tend to be stable.

V. CONCLUSION

In this paper, to more accurately characterize the losses of GMM under compressive stress, an MDOF LECM incorporating the equivalent stiffness and contact damping of the transducer contact surface and the structural losses is newly established. Thus, a novel parameter characterization method is proposed based on MDOF LECM. The comparative analysis with the classical parameter characterization methods based on DECM shows that:

1) The three losses of GMM are more sensitive to the fitness function of the proposed method, and the material losses extracted have better stability;

2) The parametric characterization results under six different compressive stresses also demonstrate the usefulness of the proposed method.

3) This study also reports the complex parameters of the GMM under compressive stress, with a focus on the variation trend of the intensive losses. The magnetic losses are shown to decrease monotonically with the compressive stress, and the elastic losses decrease monotonically in the range of 6-15Mpa, and change little after 15 Mpa. The trend of piezomagnetic losses is similar to that of elastic losses.

The proposed parameter characterization method will facilitate a more accurate FEM analysis of high-power transducers and help us further understand the loss mechanism of GMM.

APPENDIX A

According to [2], the mechanical impedance of the GMM rod, magnetic column, and displacement plunger all can be written in the form of the transmission line equation (Eq. A1),where the Z_L represents the load impedance.

$$Z_0 = \rho cA[Z_L + j\rho cA\tan kl]/[\rho cA + jZ_L\tan kl] \quad \text{(A1)}$$

According to the electromechanical analogy, the equivalent circuit model corresponding to the mechanical model of the GMM in Fig.2 (c) can be obtained, as shown in Fig.A1(a). In this study, because one end of the GMM is a clamped condition, which is equivalent to a very large ZL at one end, resulting in Eq. (11) as the impedance at the other end of the GMM. After some algebraic and trigonometric identities, it can be shown that the "T network" shown in Fig.A1 (b) is consistent with Eq. (11).

Similarly, the equivalent circuit model corresponding to the magnetic column and the displacement plunger in Fig.2(c) can be obtained, as shown in Fig. A2(a), where the subscripts *C* and *D* correspond to the magnetic column and the output rod, respectively. Because they are free conditions at both ends, and $F_{C1}/\tau_1=Z_0$ ($F_{D1}/\zeta_1=Z_0$) at port 1 and $F_{C2}/\tau_2=Z_L$($F_{D2}/\zeta_2=Z_L$) at port 2, where F is the output force. Through the calculation, the equivalent "T network" of the magnetic column and the displacement plunger is obtained as shown in Fig. A2(b), and the corresponding Eq. is (11)-(14).

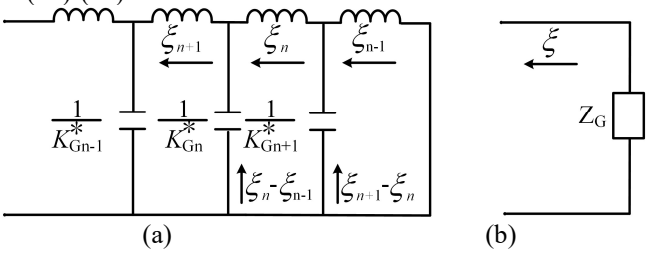

Fig.A1 Equivalent circuit (a) and Distributed T network circuit (b) of GMM

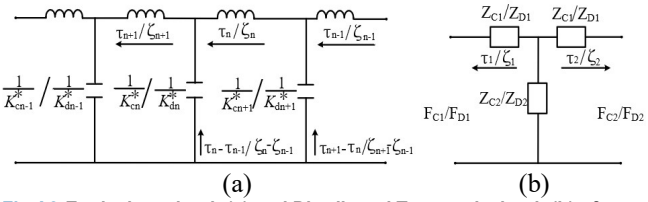

Fig.A2 Equivalent circuit (a) and Distributed T network circuit (b) of Magnetic column and displacement plunger

In summary, the DECM of the mechanical end of the transducer shown in Fig.4 can be obtained.

APPENDIX B

The parameter identification process of the PSO is the process of finding the minimum value of a fitness function. Each particle finding the global optimal particle position in the solution space by continuously updating its position and velocity through iteration [56]. The position update and velocity update formula used are (B1) and (B2), respectively

$$v_{i+1} = wv_i + c_1\cdot rand()\cdot(pbest_i - x_i) + c_2\cdot rand()\cdot(gbest_i - x_i) \quad \text{(B1)}$$

$$x_{i+1} = x_i + v_{i+1} \quad \text{(B2)}$$

where *i* is the *i*-th particle in the particle swarm of size *m* and m was set as 12 in this study. *w* is the inertia weight, c_1 and c_2 are learning factors. And *w* was set as 0.5, c_1 and c_2 are set as 2. *rand*() is a random number between 0-1 randomly generated by the system, $pbest_i$ is the optimal solution of the *i*-th generation particle; $gbest_i$ is the number of particles in all particles in the group optimal solution.

In this study, the fitness function of Method A is Equations. (19) and (20), the fitness function of Methods B and C are (21) and (22), respectively. The parameter identification process of the PSO is illustrated in Fig.B1.

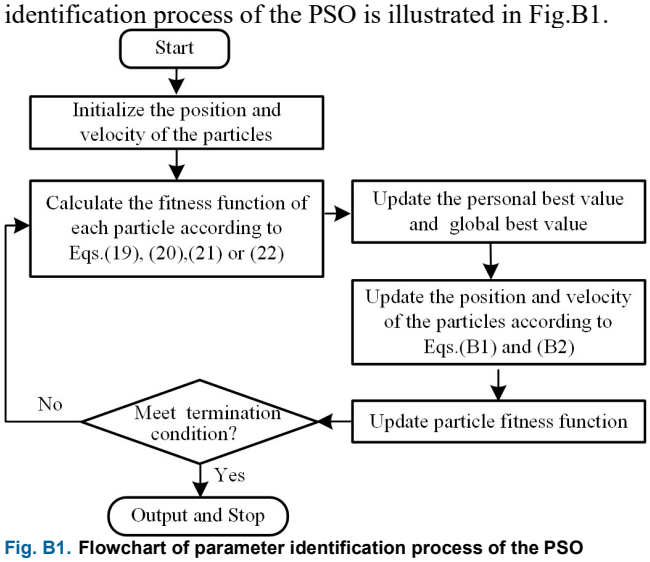

Fig. B1. Flowchart of parameter identification process of the PSO

ACKNOWLEDGMENT

This research was funded by the Huxiang High-level Talent Gathering Project, grant number 2019RS1028, for which the authors are most grateful.

REFERENCES

[1] M. Yang, X. Yang, Y. Wei, Z. Zhang, and Y. Chen, "SPICE Modeling of a High-Power Terfenol-D Transducer Considering Losses and Magnetic Flux Leakage," *IEEE Trans. Ultrason. Ferroelectr. Freq. Control*, vol. 69, no. 2, pp. 812–822, 2022, doi: 10.1109/TUFFC.2021.3132765.

[2] J. L. Butler, C. H. Sherman, and David A Brown, *Transducers and arrays for underwater sound*, Second Edi. Cham, Switzerland: Springer International Publishing, 2016.

[3] X. Sun, Z. Wang, and Y. Yang, "Design and experimental investigation of a novel compliant positioning stage with low-frequency vibration isolation capability," *Sensors Actuators, A Phys.*, vol. 295, pp. 439–449, 2019, doi: 10.1016/j.sna.2019.06.032.

[4] H. D. Gohari, M. R. Zarastvand, R. Talebitooti, A. Loghmani, and M. Omidpanah, "Radiated sound control from a smart cylinder subjected to piezoelectric uncertainties based on sliding mode technique using self-adjusting boundary layer,"

Aerosp. Sci. Technol., vol. 106, p. 106141, 2020, doi: 10.1016/j.ast.2020.106141.

[5] M. R. Zarastvand, M. Ghassabi, and R. Talebitooti, "A Review Approach for Sound Propagation Prediction of Plate Constructions," *Arch. Comput. Methods Eng.*, vol. 28, no. 4, pp. 2817–2843, 2021, doi: 10.1007/s11831-020-09482-6.

[6] X. Dong, C. Jiang, L. Jin, Z. Xu, and Y. Yuan, "Inherent Loss Analysis of Piezoelectrics in Radial Vibration and Its Application in Ultrasonic Motor," *IEEE Trans. Ultrason. Ferroelectr. Freq. Control*, vol. 67, no. 8, pp. 1632–1640, 2020.

[7] K. Uchino, *High-Power Piezoelectrics and Loss Mechanisms*, 2nd ed. Woodhead Publishing, 2017.

[8] X. Dong, K. Uchino, C. Jiang, L. Jin, Z. Xu, and Y. U. E. Yuan, "Electromechanical Equivalent Circuit Model of a Piezoelectric Disk Considering Three Internal Losses," *IEEE ACCESS*, vol. 8, 2020, doi: 10.1109/ACCESS.2020.3028698.

[9] M. Tao, Y. Zhuang, D. Chen, S. O. Ural, Q. Lu, and K. Uchino, "Characterization of magnetostrictive losses using complex parameters," *Adv. Mater. Res.*, vol. 490–495, pp. 985–989, 2012, doi: 10.4028/www.scientific.net/AMR.490-495.985.

[10] Y. Park, H. Daneshpajooh, T. Scholehwar, E. Hennig, and K. Uchino, "Partial electrode method for loss and physical parameter determination of piezoceramics: Simplification, error investigation and applicability," *J. Eur. Ceram. Soc.*, vol. 41, no. 12, pp. 5900–5908, 2021, doi: 10.1016/j.jeurceramsoc.2021.05.037.

[11] K. Uchino, *FEM and Micromechatronics with ATILA Software*. CRC Press, 2018.

[12] Y. Park, Y. Zhang, M. Majzoubi, T. Scholehwar, E. Hennig, and K. Uchino, "Improvement of the standard characterization method on k33 mode piezoelectric specimens," *Sensors Actuators, A Phys.*, vol. 312, p. 112124, 2020, doi: 10.1016/j.sna.2020.112124.

[13] T. Nakamura, I. Nakano, A. Kawamori, and T. Yoshikawa, "Static and dynamic characteristics of giant magnetostrictive materials under high pre-stress," *Japanese J. Appl. Physics, Part 1 Regul. Pap. Short Notes Rev. Pap.*, vol. 40, no. 5 B, pp. 3658–3663, 2001, doi: 10.1143/jjap.40.3658.

[14] M. Domenjoud, E. Berthelot, N. Galopin, R. Corcolle, Y. Bernard, and L. Daniel, "Characterization of giant magnetostrictive materials under static stress: Influence of loading boundary conditions," *Smart Mater. Struct.*, vol. 28, no. 9, 2019, doi: 10.1088/1361-665X/ab313b.

[15] R. D. Greenough, I. M. Reed, K. C. O'Connor, A. Wharton, and M. P. Schulze, "The characterisation of transducer materials," *Ferroelectrics*, vol. 187, no. 1–4, pp. 129–140, 1996, doi: 10.1080/00150199608244849.

[16] I. M. Reed, R. D. Greenough, and A. G. I. Jenner, "Frequency Dependence Of The Piezomagnetic Strain Coefficient," *IEEE Trans. Magn.*, vol. 31, no. 6, pp. 4038–4040, 1995, doi: 10.1109/20.489854.

[17] R. D. Greenough and A. D. Wharton, "Methods and techniques to characterise Terfenol-D," *J. Alloys Compd.*, vol. 258, no. 1–2, pp. 114–117, 1997, doi: 10.1016/s0925-8388(97)00079-0.

[18] H. Daneshpajooh, M. Choi, Y. Park, T. Scholehwar, E. Hennig, and K. Uchino, "Compressive stress effect on the loss mechanism in a soft piezoelectric Pb(Zr,Ti)O3," *Rev. Sci. Instrum.*, vol. 90, no. 7, p. 075001,July., 2019, doi: 10.1063/1.5096905.

[19] Stefan Johann Rupitsch, *Piezoelectric sensors and actuators: Fundamentals and applications*. Berlin, Germany: Springer-Verlag GmbH Germany, 2019.

[20] M. G. Cain, P. Jirˇí Tesarˇ, and Marijn van Veghel, *Characterisation of ferroelectric bulk materials and thin films*. The Netherlands: Springer, 2014.

[21] M. R. Karafi and F. Khorasani, "Evaluation of mechanical and electric power losses in a typical piezoelectric ultrasonic transducer," *Sensors Actuators, A Phys.*, vol. 288, pp. 156–164, 2019, doi: 10.1016/j.sna.2018.12.044.

[22] A. Abdullah and M. Malaki, "On the damping of ultrasonic transducers' components," *Aerosp. Sci. Technol.*, vol. 28, no. 1, pp. 31–39, 2013, doi: 10.1016/j.ast.2012.10.002.

[23] Q. Lu and X. Chen, "Application of piezoelectric actuator in series nano-positioning stage," *Sci. Prog.*, vol. 103, no. 1, pp. 1–14, 2020, doi: 10.1177/0036850419892190.

[24] R. Talebitooti, H. Darvish Gohari, M. Zarastvand, and A. Loghmani, "A robust optimum controller for suppressing radiated sound from an intelligent cylinder based on sliding mode method considering piezoelectric uncertainties," *J. Intell. Mater. Syst. Struct.*, vol. 30, no. 20, pp. 3066–3079, 2019, doi: 10.1177/1045389X19873412.

[25] M. H. Asadijafari, M. R. Zarastvand, and R. Talebitooti, "The effect of considering Pasternak elastic foundation on acoustic insulation of the finite doubly curved composite structures," *Compos. Struct.*, vol. 256, p. 113064, 2021, doi: 10.1016/j.compstruct.2020.113064.

[26] H. Darvishgohari, M. R. Zarastvand, R. Talebitooti, and R. Shahbazi, "Hybrid control technique for vibroacoustic performance analysis of a smart doubly curved sandwich structure considering sensor and actuator layers," *J. Sandw. Struct. Mater.*, vol. 23, no. 5, pp. 1453–1480, 2021, doi: 10.1177/1099636219896251.

[27] X. Li, R. Sriramdas, Y. Yan, M. Sanghadasa, and S. Priya, "A New Method for Evaluation of the Complex Material Coefficients of Piezoelectric Ceramics in the Radial Vibration Modes," *IEEE Trans. Ultrason. Ferroelectr. Freq. Control*, vol. 68, no. 11, pp. 3446–3460, 2021.

[28] X. Yang, Y. Liu, W. Chen, and J. Liu, "Sandwich-Type Multi-Degree-of-Freedom Ultrasonic Motor with Hybrid Excitation," *IEEE Access*, vol. 4, pp. 905–913, 2016, doi: 10.1109/ACCESS.2016.2536611.

[29] B. Ju, Z. Guo, Y. Liu, G. Qian, L. Xu, and G. Li, "Self-Sensing Vibration Suppression of Piezoelectric Cantilever Beam Based on Improved Mirror Circuit," *IEEE Access*, vol. 7, pp. 148381–148392, 2019, doi: 10.1109/ACCESS.2019.2946722.

[30] S. Sarangapani and X. Yan, "Improvement in the Electromechanical Properties of a Partially Diced Piezoelectric Disc Transducer," *IEEE Access*, vol. 6, pp. 70324–70330, 2018, doi: 10.1109/ACCESS.2018.2879463.

[31] K. W. Kwok, H. Lai, W. Chan, and C. L. Choy, "Evaluation of the material parameters of piezoelectric materials by various methods," *IEEE Trans. Ultrason. Ferroelectr. Freq. Control*, vol. 44, no. 4, pp. 733–742, 1997, doi: 10.1109/58.655188.

[32] Y. Dong, Z. Wu, H. Hu, B. Wu, and G. Xu, "A Novel Method for Characterization of Piezoelectric Material Parameters by Simulated Annealing Optimization," *IEEE Trans. Ultrason. Ferroelectr. Freq. Control*, vol. 57, no. 12, pp. 2613–2615, 2010, doi: 10.1109/TUFFC.2010.1735.

[33] X. Sun *et al.*, "A novel characterization method of piezoelectric composite material based on particle swarm optimization algorithm," *Appl. Math. Model.*, vol. 66, pp. 322–331, 2019, doi: 10.1016/j.apm.2018.08.015.

[34] M. Wild, M. Bring, H. Lars, and K. Hjelmervik, "Characterization of Piezoelectric Material Parameters Through a Global Optimization Algorithm," *Ieee J. Ocean. Eng.*, vol. 45, no. 4, pp. 480–488, 2020, doi: 10.1109/JOE.2018.2882262.

[35] S. J. Rupitsch and J. Ilg, "Complete characterization of piezoceramic materials by means of two block-shaped test samples," *IEEE Trans. Ultrason. Ferroelectr. Freq. Control*, vol. 62, no. 7, pp. 1403–1413, 2015, doi: 10.1109/TUFFC.2015.006997.

[36] N. Pérez, R. C. Carbonari, M. A. B. Andrade, F. Buiochi, and J. C. Adamowski, "A FEM-based method to determine the complex material properties of piezoelectric disks," *Ultrasonics*, vol. 54, no. 6, pp. 1631–1641, 2014, doi: 10.1016/j.ultras.2014.03.006.

[37] S. Sherrit, H. D. Wiederick, B. K. Mukherjee, and M. Sayer, "An accurate equivalent circuit for the unloaded piezoelectric vibrator in the thickness mode," *J. Phys. D. Appl. Phys.*, vol. 30, no. 16, pp. 2354–2363, 1997.

[38] X. Du, Q. Wang, and K. Uchino, "An Accurate Method for the Determination of Complex Coefficients of Single Crystal Piezoelectric Resonators II : Design of Measurement and Experiments," *IEEE Trans. Ultrason. Ferroelectr. Freq. Control*, vol. 51, no. 2, pp. 238–248, 2004, doi: 10.1109/TUFFC.2004.1295399.

[39] S. Sherrit, T. J. Masys, H. D. Wiederick, and B. K. Mukherjee, "Determination of the reduced matrix of the piezoelectric, dielectric, and elastic material constants for a piezoelectric material with C∞ symmetry," *IEEE Trans. Ultrason. Ferroelectr. Freq. Control*, vol. 58, no. 9, pp. 1714–1720, 2011, doi: 10.1109/TUFFC.2011.2008.

[40] R. G. Sabat, B. K. Mukherjee, W. Ren, and G. Yang, "Temperature dependence of the complete material coefficients matrix of soft and hard doped piezoelectric lead zirconate titanate ceramics," *J. Appl. Phys.*, vol. 101, no. 6, pp. 121–126, 2007, doi: 10.1063/1.2560441.

[41] Q. M. Zhang, J. Zhao, K. Uchino, and J. Zheng, "Change of the weak-field properties of Pb(ZrTi)O3 piezoceramics with compressive uniaxial stresses and its links to the effect of dopants on the stability of the polarizations in the materials," *J. Mater. Res.*, vol. 12, no. 1, pp. 226–234, 1997, doi: 10.1557/JMR.1997.0030.

[42] Y. Chen, X. Yang, M. Yang, Y. Wei, and H. Zheng, "Characterization of giant magnetostrictive materials using three complex material parameters by particle swarm optimization," *Micromachines*, vol. 12, no. 11, p. 1416,Nov., 2021, doi: 10.3390/mi12111416.

[43] G. Engdahl, "Design Procedures For Optimal Use Of Giant Design Procedures For Optimal Use Of Giant Magnetostrictive Materials In Magnetostrictive Materials In Magnetostrictive Actuator Applications Magnetostrictive Actuator Applications," in *Actuator 2002, 8th International Conference on New Actuators*, 2002, no. June, pp. 10–12.

[44] G. Lan, W. Sun, X. Zhang, Y. Chen, W. Tan, and X. Li, "A three-dimensional fractal model of the normal contact characteristics of two contacting rough surfaces," *AIP Adv.*, vol. 11, no. 5, 2021, doi: 10.1063/5.0045151.

[45] P. Liu, H. Zhao, K. Huang, and Q. Chen, "Research on normal contact stiffness of rough surface considering friction based on fractal theory," *Appl.*

Surf. Sci., vol. 349, pp. 43–48, 2015, doi: 10.1016/j.apsusc.2015.04.174.

[46] D. Zhang, Y. Xia, F. Scarpa, J. Hong, and Y. Ma, "Interfacial contact stiffness of fractal rough surfaces," *Sci. Rep.*, vol. 7, no. 1, pp. 1–9, 2017, doi: 10.1038/s41598-017-13314-2.

[47] Y. Zhao, J. Xu, L. Cai, W. Shi, and Z. Liu, "Stiffness and damping model of bolted joint based on the modified three-dimensional fractal topography," *Proc. Inst. Mech. Eng. Part C J. Mech. Eng. Sci.*, vol. 231, no. 2, pp. 279–293, 2017, doi: 10.1177/0954406216631577.

[48] Y. Yuan, Y. Cheng, K. Liu, and L. Gan, "A revised Majumdar and Bushan model of elastoplastic contact between rough surfaces," *Appl. Surf. Sci.*, vol. 425, pp. 1138–1157, 2017, doi: 10.1016/j.apsusc.2017.06.294.

[49] C. Rong, Z. He, D. Li, Z. Yang, and G. Xue, "Dynamic modeling and analysis of stack giant magnetostrictive actuator," *Sensors Actuators, A Phys.*, vol. 276, pp. 205-218,Apr., 2018, doi: 10.1016/j.sna.2018.04.020.

[50] D. L. Hall, "Dynamics and vibration of magnetostrictive transducers," 1994.

[51] S. W.Meeks, "A mobility analogy equivalent circuit of a magnetostrictive transducer in the presence of eddy currents," *J. Acoust. Soc. Am.*, vol. 67, no. 2, pp. 683–692, 1980, doi: 10.1121/1.383894.

[52] A. Saltelli, "Sensitivity analysis for importance assessment," no. I, pp. 1–21, 2002, doi: 10.1111/0272-4332.00040.

[53] A. Saltelli, M. Ratto, F. Campolongo, J. Cariboni, and D. Gatelli, *Global Sensitivity Analysis . The Primer Global Sensitivity Analysis . The Primer*. 2008.

[54] A. Gopal, M. M. Sultani, and J. C. Bansal, "On Stability Analysis of Particle Swarm Optimization Algorithm," *Arab. J. Sci. Eng.*, vol. 45, no. 4, pp. 2385–2394, 2020, doi: 10.1007/s13369-019-03991-8.

[55] M. J. Dapino, A. B. Flatau, and F. T. Calkins, "Statistical analysis of Terfenol-D material properties," *J. Intell. Mater. Syst. Struct.*, vol. 17, no. 7, pp. 587–599, 2006, doi: 10.1177/1045389X06059500.

[56] James Kennedy and Russell Eberhart, "Particle Swarm Optimization," *Part. Swarm Optim.*, pp. 1942–1948, 1995